

Supplemental Material: "Nematicity-enhanced superconductivity in systems with a non-Fermi liquid behavior"

Sharareh Sayyad,^{1,2,*} Motoharu Kitatani^{a,3} Abolhassan Vaezi^{a,4,†} and Hideo Aoki^{5,6}

¹*Univ. Grenoble Alpes, CNRS, Grenoble INP, Institut Néel, Grenoble 38000, France*

²*Max Planck Institute for the Science of Light, Staudtstraße 2, 91058 Erlangen, Germany*

³*RIKEN Center for Emergent Matter Sciences (CEMS), Wako, Saitama, 351-0198, Japan[‡]*

⁴*Department of Physics, Sharif University of Technology, Tehran 14588-89694, Iran[‡]*

⁵*Department of Physics, University of Tokyo, Hongo, Tokyo 113-0033, Japan*

⁶*Electronics and Photonics Research Institute, Advanced Industrial Science and Technology (AIST), Tsukuba, Ibaraki 305-8568, Japan*

We explore the interplay between nematicity (spontaneous breaking of the sixfold rotational symmetry), superconductivity, and non-Fermi liquid behavior in partially flat-band models on the triangular lattice. A key result is that the nematicity (Pomeranchuk instability), which is driven by many-body effect and stronger in flat-band systems, enhances superconducting transition temperature in a systematic manner on the T_c dome. There, a plausible $s_{x^2+y^2} - d_{x^2-y^2} - d_{xy}$ -wave symmetry, in place of the conventional $d_{x^2-y^2}$ -wave, governs the nematicity-enhanced pairing with a sharp rise in the T_c dome on the filling axis. When the sixfold symmetry is spontaneously broken, the pairing interaction is shown to become stronger with more compact pairs in real space than when the symmetry is enforced. These are accompanied by a non-Fermi character of electrons in the partially flat bands with many-body interactions.

INTRODUCTION

Strongly correlated systems have become an epitome in the condensed-matter physics, as exemplified by the high-temperature superconductivity in the cuprate [1], and iron-based [2] families. These compounds exhibit rich phase diagrams as hallmarked by the emergence of unconventional superconductivity, and a plethora of symmetry-broken phases such as spin and charge nematicity and stripe orders.

Quest for finding novel high-temperature superconductors spurs interests in exploring many-body systems with short-range repulsions but with (nearly) flat subregions in the band dispersion arising from hopping beyond nearest neighbors or from lattice structures [3, 4]. These systems with dispersionless band portions permit numerous scattering channels for the electrons and can give rise to various exotic quantum phases such as spin and charge density waves [5, 6], Mott insulating [7], and bad-metallic phases [8], as well as the formation of spatially extended Cooper pairs [9, 10].

Interaction and the flatness of the band structure can be intimately related to geometric and quantum frustration in producing strong correlation effects. The spin liquid behavior in hexagonal lattices, such as organic compounds [11, 12]) and inorganic Herbertsmithites [13, 14], are typical examples. In these exotic liquids, the classical picture is no longer valid, and their quantum phase transitions cannot be described within Landau's phase transition theory.

Aside from these many-body phenomena, the electron nematicity, i.e., spontaneous breaking of spatial rotational symmetry triggered by many-body interactions, is another manifestation of the correlation effects [15, 16].

It is an intriguing direction to pursue the physical origins of these symmetry-broken phases [17–19], and to grasp the interplay between nematicity and other phases such as superconductivity [10, 20–23] and non-Fermi liquid [24]. Various studies report different roles of nematic fluctuations on the superconductivity including the competition between these two phases, e.g., in doped BaFe_2As_2 [25], the assistance of nematicity to enhance the superconductivity transition temperature, e.g., in twisted bilayer graphene [26], and the negligible effect of nematicity on the superconducting phase, e.g., in FeSe [27]. One crucial aspect is figuring out which of these possibilities occur in systems that have a flat or partially flat band in their dispersions [5, 6, 28, 29].

In this paper, we bring these features together to explore the interplay between the nematicity and superconductivity in partially flat band (PFB) models on the triangular lattice, effective model for Moire-produced basis states [30]. Here the lattice structure frustrates magnetic orders, thereby giving opportunities for nematic instabilities to arise. As a key finding, we shall demonstrate that nematicity can significantly enhance transition temperatures (T_c) in the superconducting phase, with a $s_{x^2+y^2} - d_{x^2-y^2} - d_{xy}$ -wave pairing symmetry. This occurs for an intermediate Hubbard repulsion and in a non-Fermi liquid regime.

MODEL

The Hubbard Hamiltonian on the isotropic triangular lattice reads

$$H = \sum_{\mathbf{k}, \sigma} \varepsilon_{\mathbf{k}} c_{\mathbf{k}\sigma}^\dagger c_{\mathbf{k}\sigma} + U \sum_i n_{i\uparrow} n_{i\downarrow} - \mu \sum_{i\sigma} n_{i\sigma}, \quad (1)$$

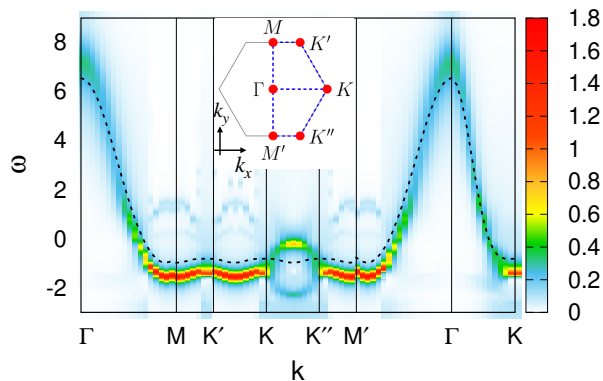


Figure 1. Momentum-dependent spectral function along high-symmetry momenta [see labels in the inset] in the PFB system with $t' = 0.15$ for $\langle n \rangle = 0.9$ and $U = 4.5$. Dashed black lines in each panel represents the shifted noninteracting band structure ($\varepsilon_{\mathbf{k}} - \mu$) with a chemical potential $\mu = -0.9$. (Inset) Hexagonal Brillouin zone for the triangular lattice with high symmetry points marked, i.e., Γ at $(k_x, k_y) = (0, 0)$, K at $(4\pi/3, 0)$, K' at $(2\pi/3, 2\pi\sqrt{3}/3)$, K'' at $(2\pi/3, -2\pi\sqrt{3}/3)$, M at $(0, 2\pi\sqrt{3}/3)$, and M' at $(0, -2\pi\sqrt{3}/3)$. M and M' are equivalent, in both of twofold (in the presence of the nematicity) and sixfold (in its absence) rotational symmetries. In the presence of sixfold symmetry, K' and K'' are equivalent as well.

where $c_{\mathbf{k}\sigma}^\dagger$ ($c_{\mathbf{k}\sigma}$) creates (annihilates) an electron with momentum $\mathbf{k} = (k_x, k_y)$ and spin σ at site i , $n_{i\sigma} \equiv c_{i\sigma}^\dagger c_{i\sigma}$. The repulsive Hubbard interaction is denoted as $U (> 0)$, and μ is the chemical potential. The non-interacting band dispersion for the triangular lattice is given as

$$\varepsilon_{\mathbf{k}}(t, t') = -t \left[-2 \cos(k_x) - 4 \cos(k_x/2) \cos(\sqrt{3}k_y/2) \right] + t' \left[-2 \cos(\sqrt{3}k_y) - 4 \cos(3k_x/2) \cos(\sqrt{3}k_y/2) \right], \quad (2)$$

where t is the nearest-neighbor hopping (taken as a unit of energy) and t' is the second-neighbor hopping. Here, we consider $(t, t') = (1.0, 0.15)$, which possesses a nearly flat region along $K - K' - K''$, see dashed line in Fig. 1. For the interaction, we set an intermediate $U = 4.5t$, with the inverse temperature set to be $\beta \equiv 1/(k_B T) = 30/t$ except in Fig. 3(c).

NUMERICAL METHOD

To study paramagnetic phases with no spin imbalance, we employ the dynamical mean-field theory (DMFT) combined with the fluctuation exchange approximation (FLEX), known as the FLEX+DMFT [31]. This method comprises DMFT and FLEX double loops, solved self-consistently at each FLEX+DMFT iteration. In this work, we solve the DMFT impurity problem by the modified iterative perturbation theory [32, 33]. The momentum-dependent FLEX self-energy is constructed from the bubble and ladder diagrams. Af-

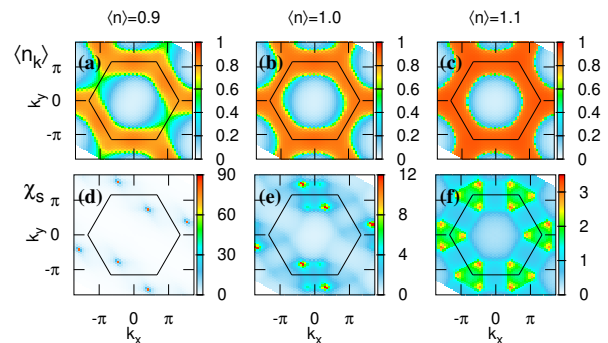


Figure 2. Momentum distribution functions (top panels) and spin susceptibilities (bottom) are displayed in momentum space for band fillings $\langle n \rangle = 0.9$ (a, d), 1.0 (b, e), and 1.1 (c, f). All results are calculated for the PFB systems with $t' = 0.15$ and $U = 4.5$. The black hexagon in each panel indicates the Brillouin zone. Note different color bars between different band fillings.

ter removing the doubly-counted diagrams in the local FLEX self-energy, the FLEX+DMFT self-energy is updated. The momentum-dependent self-energy in the FLEX+DMFT incorporates vertex corrections generated from the DMFT iterations into the local part of the FLEX self-energy. Even though our FLEX+DMFT method does not deal with spatial vertex corrections, larger coordination number and frustrated magnetic fluctuations in the triangular lattice give rise to more local self-energies and less dominant spatial vertex corrections than in the square lattice [34]. As a result, the FLEX+DMFT is considered to be a reliable approach that incorporates local and nonlocal correlations.

When we start from the non-interacting tight-binding Hamiltonian, Eq. (1), that has the sixfold rotational (C_6) lattice symmetry, the solution of the many-body problem may exhibit a lower the symmetry. To study the phases with/without C_6 symmetry, we solve the FLEX+DMFT loops with/without imposing the C_6 constraints. To explore the Pomeranchuk instability with the broken C_6 symmetry, we take an initial self-energy as $\Sigma_{\text{in}} = 0.05[\cos(k_x) - \cos(\sqrt{3}k_y/2) \cos(k_x/2)]$ which acts as a seed for distorting the Fermi surface for the FLEX+DMFT iterations. The FLEX+DMFT calculations are here performed on a 64×64 momentum grid and an energy mesh with 2048 points.

NEMATICITY AND NON-FERMI LIQUID BEHAVIOR

We start with presenting the momentum distribution function plotted in panels (a-c) in Fig. 2(top rows). For a system with a well-defined Fermi surface, $\langle n_{\mathbf{k}} \rangle$ should take the value of unity (zero) inside (outside) the Fermi surface for $T \rightarrow 0$. For all band fillings in our results,

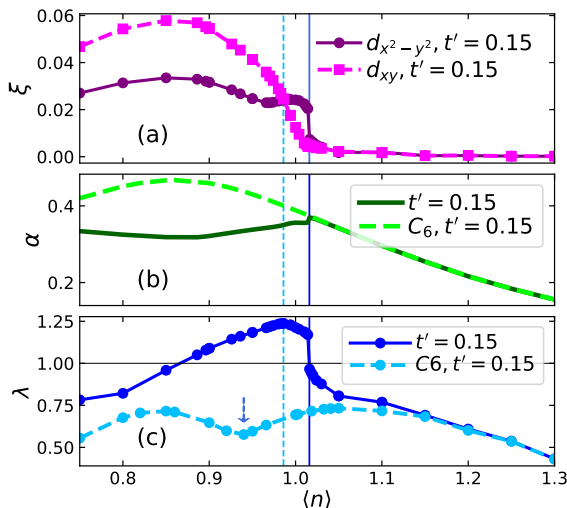


Figure 3. (a) Pomeranchuk order parameter ξ . $\xi_{d_{x^2-y^2}}$ for $t' = 0.15$ is represented by purple lines. $\xi_{d_{xy}}$ is shown by magenta lines. (b) Exponent α of the impurity self-energy for systems with (dashed curves) and without (solid) imposed sixfold symmetry. (c) The largest eigenvalue λ of the linearized Eliashberg equation for the singlet pairing symmetry against band filling for the PFB system with $t' = 0.15$ and $U = 4.5$, with the broken (dark blue curves) or unbroken (sky-blue) sixfold symmetry. black horizontal line marks $\lambda = 1$, and an arrow points to the dip in λ when C_6 is enforced. Vertical blue solid lines indicate $\langle n_{c_1} \rangle$ (see text). Vertical dotted sky-blue lines are at $\langle n_{c_1} \rangle = \langle n_{c_2} \rangle$.

the maxima of the momentum-dependent distribution function are below unity. The system exhibits a filling-dependent degrading of C_6 down to a twofold C_2 symmetry in $\langle n_k \rangle$. Namely, we have here an emergence of nematicity, or a *Pomeranchuk instability*. The breaking of C_6 is seen to occur even right at half-filling, while the electron-doped case shows a preserved C_6 .

To quantify the broken C_6 symmetry, we introduce point-group resolved Pomeranchuk order parameters defined as $\xi_{d_{x^2-y^2}} = \sum_{\mathbf{k}} d_{x^2-y^2}(\mathbf{k})n_{\mathbf{k}}$ and $\xi_{d_{xy}} = \sum_{\mathbf{k}} d_{xy}(\mathbf{k})n_{\mathbf{k}}$, with $\sum_{\mathbf{k}} = 1$ [35]. The form factors, $d_{x^2-y^2} = \cos(k_x) - \cos(\sqrt{3}k_y/2)\cos(k_x/2)$ and $d_{xy} = \sqrt{3}\sin(\sqrt{3}k_y/2)\sin(k_x/2)$, describe the distortion of the Fermi surface in the point group C_6 , and ξ is a real number with values between zero (when C_6 is preserved) and unity.

Figure 3(a) displays ξ against the band filling. We can see that, as the band filling is reduced, ξ starts to grow, and at a critical band filling $\langle n_{c_1} \rangle = 1.02$ [vertical blue line in Fig. 3(a)], $\xi_{d_{xy}}$ undergoes a first-order phase transition [36, 37]. At this filling, the onset of nematicity is accompanied by a Lifshitz transition, where the Fermi surface delineated by the ridges in $|G_{\mathbf{k}}|^2$ (not shown) is not only distorted but undergoes a topological change from closed to open structures.

We further notice that the filling dependence of the

nematicity differs between $\xi_{d_{x^2-y^2}}$ and $\xi_{d_{xy}}$ in the PFB model; compare purple and magenta lines in Fig. 3(a). For $0.986 < \langle n \rangle < \langle n_{c_1} \rangle$, $\xi_{d_{x^2-y^2}}$ is dominant, while $\xi_{d_{xy}}$ takes over below $\langle n \rangle = 0.986$, which we call the second characteristic band filling, $\langle n_{c_2} \rangle$ [vertical dashed sky-blue line in Fig. 3(a)]. While $\xi_{d_{x^2-y^2}}$ displays a first-order transition at $\langle n_{c_1} \rangle$, $\xi_{d_{xy}}$ exhibits a crossover at $\langle n_{c_2} \rangle$. This suggests that thermodynamic parameters such as temperature at which $\xi_{d_{xy}}$ and $\xi_{d_{x^2-y^2}}$ experience the first-order transitions are different from each other.

To trace back the origin of the nematic phases, let us next present the momentum-dependent spin susceptibility $\chi_s(\mathbf{k})$ for the PFB model in Fig. 2(d-f). In the electron-doped regime where the Pomeranchuk instability is absent, χ_s respects the sixfold rotational symmetry of the lattice, with peaks at $\mathbf{k} = (\sqrt{3}\pi/2, 0)$ and its equivalent positions under C_6 . As band filling is decreased below the half-filling, the spin susceptibility develops spikes around $\mathbf{k} = (\sqrt{3}\pi/3, 2\pi/3)$ and the equivalent places under a C_2 subgroup of the original C_6 rotational symmetry. The appearance of spikes at mid-momenta in the spin susceptibilities indicates the presence of long-range spin fluctuations in our systems [38].

In general, an electronic nematicity without breaking the translational symmetry can be driven by structural transitions, charge [39] or spin [40] fluctuations. Our Hamiltonian does not deal with the distortion of the lattice or phonons and thus precludes structural transitions. We have checked that the charge susceptibility is at least an order of magnitude smaller than the spin susceptibility. Thus the spin-mediated correlations should be responsible for the emergence of the Pomeranchuk instability [41].

Now let us turn to a non-Fermi liquid character of the present electronic systems, since the flat portions of the band may well exert peculiar effects. We can quantify this in terms of the impurity self-energy in DMFT by fitting the imaginary part of the self-energy on Matsubara axis to $|\text{Im}\Sigma_{\text{DMFT}}(i\omega_n)| \propto \omega_n^\alpha$, and present the result for the exponent α in Fig. 3(b). In general, $\alpha = 1$ at small ω_n (c.f., $\alpha = 2$ on real frequency axis as $|\text{Im}\Sigma_{\text{DMFT}}(\omega)| \approx \max(\omega^2, T^2)$ at small T) characterizes the Fermi liquid, while $\alpha < 0.5$ will signify a non-Fermi liquid (bad metal) behavior [42–45]. Above the first order Pomeranchuk transition for $\langle n \rangle > \langle n_{c_1} \rangle$, α 's computed for systems with (dashed lines) and without (solid lines) the enforced C_6 constraint trivially coincide with each other. We can see that both systems display strong non-Fermi liquid behavior with α well below 1. If we turn to $\langle n \rangle < \langle n_{c_1} \rangle$ for which we have revealed the nematicity, Fig. 3(b) shows notable differences in α between the cases where C_6 is enforced or not. After a sharp drop at $\langle n_{c_1} \rangle$ as the band filling is reduced, α gradually increases (decreases) in the presence (absence) of the imposed sixfold constraint. Eventually α starts to decrease with deas-

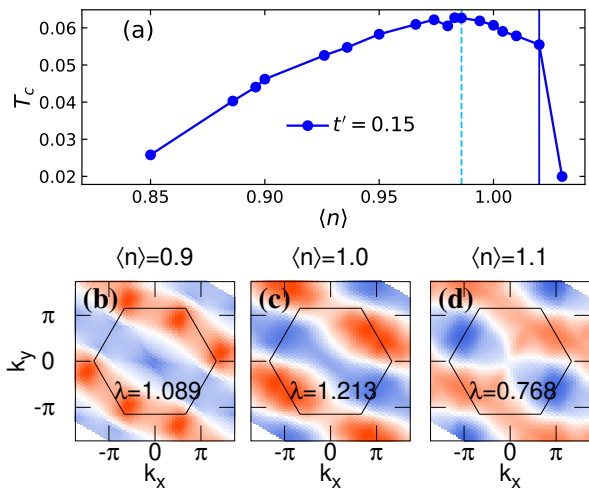


Figure 4. (a) Superconducting transition temperature T_c against band filling for the PFB. Vertical solid line indicates $\langle n_{c1} \rangle$, while vertical dotted line indicates $\langle n \rangle = \langle n_{c2} \rangle$. (b-d) Gap functions in momentum-space with singlet pairing for the PFB system with $t' = 0.15$ for $U = 4.5$ and $\beta = 30$ for $\langle n \rangle = 0.9$ (a), 1.0 (b) and 1.1 (c). Black hexagons indicate the Brillouin zone. Color code for the gap function is bluish (reddish) for negative (positive) values, for which we have omitted the color bars since the linearized Eliashberg equation does not indicate magnitudes of Δ .

ing $\langle n \rangle$ at $\langle n \rangle \approx 0.85$ in the PFB system. The persistent $\alpha < 0.5$ for $\langle n \rangle < \langle n_{c1} \rangle$ implies that the nematic phase resides in the non-Fermi liquid regime.

SUPERCONDUCTIVITY

Now let us come to our key interest in pairing instabilities, for which we solve the linearized Eliashberg equation, $\lambda \Delta(k) = -\frac{1}{\beta} \sum_{k'} V_{\text{eff}}(k-k') G_{k'} G_{-k'} \Delta(k')$, to find the largest eigenvalue λ for the spin-singlet, even-frequency superconducting gap function Δ . Here, $k \equiv (\mathbf{k}, i\omega_n)$ with ω_n the fermionic Matsubara frequency, and the effective interaction for singlets given as $V_{\text{eff}}(k) = U + 3U^2 \chi_s(k)/2 - U^2 \chi_c(k)/2$. The pairing is identified when λ exceeds unity [46]. Figure 3(c) depicts λ in the presence (dashed green lines) or absence (solid blue) of imposed C_6 symmetry in PFB.

When the sixfold rotational symmetry is enforced, we get $\lambda < 0.8$ in PFB model, indicating that the singlet superconductivity does not arise for the temperature ($k_B T = t/30$) considered here. We can still notice that λ displays a double-peak structure with a minimum at $\langle n \rangle_{\text{min}} = 0.95$. The dip is shown to occur at the band filling at which the $d_{x^2-y^2}$ gap function with two-nodal lines for $\langle n \rangle > \langle n \rangle_{\text{min}}$ changes into a more complicated multi-nodal-line gap functions for $\langle n \rangle < \langle n \rangle_{\text{min}}$, see [47, 48] for details. This behavior of the gap function reflects a crossover from the antiferromagnetic spin structure with

a single nesting vector for $\langle n \rangle > \langle n \rangle_{\text{min}}$, to a more complex spin structure for $\langle n \rangle < \langle n \rangle_{\text{min}}$ where single peaks in the spin susceptibility evolve into extended structures [see Fig. 2(d-f)]. Thus the system for $\langle n \rangle < \langle n \rangle_{\text{min}}$ goes beyond the conventional nesting physics. Similar structure in λ and associated gap function have also been reported for PFB systems on the square lattice [9], again in the absence of nematicity.

In a dramatic contrast, if we allow the C_6 symmetry to be broken spontaneously, λ soars from those with C_6 restriction, as seen for $\langle n_c \rangle < \langle n \rangle < 1.15$. This occurs concomitantly with the Pomeranchuk order parameters (ξ 's), which grow precisely in this filling region. Just below $\langle n_c \rangle$, λ in the systems with broken C_6 (solid blue lines in Fig. 3 (c)) exhibits a rapid growth and exceeds unity. This is inherited in the superconducting transition temperatures (T_c), presented in Fig. 4(a).

T_c , with the broken C_6 , exhibits a single-dome structure as a function of band filling. We can observe that the presence of a flat portion in PFB or a van Hove singularity for $t' = 0$ have similar effects on the largest values of T_c when $\xi_{d_{xy}} \geq \xi_{d_{x^2-y^2}}$. One should note that, while a van Hove singularity at E_F only occurs at a single point on the filling axis, a flat portion of the band can accommodate a range of band filling. This difference is reflected in the width of the T_c dome at a given temperature; see Fig. 4(a) and SM [48]. The maximum of T_c in the PFB is seen to take place close to $\langle n_{c2} \rangle$ at which $\xi_{d_{xy}}$ exceeds $\xi_{d_{x^2-y^2}}$. Note that the superconducting transition temperature becomes almost doubled as we pass through $\langle n_{c1} \rangle$, see Fig. 4(a), which should come from the interplay between nematicity, spin fluctuations, and superconductivity.

Let us now delve into the gap function in momentum space in Fig. 4(b-d). In the electron-doped regime, the PFB model exhibits a conventional $d_{x^2-y^2}$ pairing symmetry [49]. This behavior of the gap function persists for $\langle n \rangle > \langle n_c \rangle$. On the other hand, below $\langle n_{c1} \rangle$ where the C_6 symmetry is broken down to its C_2 subgroup, the dominant channel of instability is a mixture of $s_{x^2+y^2}$, $d_{x^2-y^2}$ and d_{xy} -wave symmetries, see Fig.S16 in SM [48].

To better understand the role of nematicity in superconducting phases, we can look at $\Delta V_{\text{eff}} = V_{\text{eff}} - V_{\text{eff}}^{C_6}$, where $V_{\text{eff}}^{C_6}$ is the effective interaction with the imposed C_6 constraint. As shown in Fig. S19 in SM [48], V_{eff} is much *intensified* when C_6 is lifted. Since χ_c is much smaller than χ_s , the effective pairing interaction reflects the momentum-dependence of the spin-susceptibility under the Pomeranchuk distortions. This effective interaction assists electrons to nonlocally form Cooper pairs [15, 37, 50]. The deformation in ΔV_{eff} allows first-order perturbation corrections in the distortion, which should be responsible for the drastic changes in λ below $\langle n_c \rangle$. This contrasts with the previous study on the interplay between nematicity and superconductivity, where the enhancement of λ originates from the second-order

perturbation corrections and thus results in much smaller changes [41].

DISCUSSION AND SUMMARY

We have studied whether and how an emergent nematicity affects superconductivity in partially flat bands on the regular triangular lattice. We have shown with the FLEX+DMFT that nematicity dramatically affects pairing symmetry, and the T_C is significantly enhanced by the lowered point-group symmetry in the electronic structure. This is shown to occur in a non-Fermi liquid regime, which is characterized by blurred Fermi surfaces, momentum-dependent fractional occupations of the band, and a fractional power-law in the self-energy. In the presence of nematic order, the superconducting symmetry changes from an (extended) $d_{x^2-y^2}$ -wave to a $s_{x^2+y^2}-d_{x^2-y^2}-d_{xy}$ -wave, where unlike the conventional nesting-driven case, the pairing interaction is governed by an intricate spin susceptibility structure.

Future works should include the elaboration of the way in which the non-Fermi liquid property affects the superconductivity, and exploration of the interplay between Pomeranchuk instability and superconductivity in multi-band/orbital systems with flat regions.

ACKNOWLEDGEMENTS

Sh.S. acknowledges financial support from the ANR under the grant ANR-18-CE30-0001-01 (TOPO-DRIVE) and the European Union Horizon 2020 research and innovation program under grant agreement No.829044 (SCHINES). M.K was supported by JSPS KAKENHI Grand Numbers JP20K22342 and JP21K13887. H.A. thanks CREST (Core Research for Evolutional Science and Technology) ‘‘Topology’’ project (Grant Number JPMJCR18T4) from Japan Science and Technology Agency, and JSPS KAKENHI Grant JP17H06138.

Appendix A: Observables

Let us define the observables.

DMFT and momentum-dependent spectral functions: The DMFT spectral function, $A(\omega) = -1/\pi \text{Im}[G_{\text{imp}}(\omega)]$, is computed by analytically continuing the DMFT impurity Green’s function on Matsubara frequency axis with the Padé approximation [51]. Similarly, the momentum-dependent FLEX spectral function, $A(\mathbf{k}, \omega) = -1/\pi \text{Im}[G(\mathbf{k}, \omega)]$, is evaluated from the momentum-dependent Green’s function with an analytical continuation.

Normalized double-occupancy, $\langle n_{\uparrow}n_{\downarrow} \rangle / (\langle n_{\uparrow} \rangle \langle n_{\downarrow} \rangle)$, is the ratio between the number of doubly occupied sites $\langle n_{\uparrow}n_{\downarrow} \rangle$ to the uncorrelated value $\langle n_{\uparrow} \rangle \langle n_{\downarrow} \rangle$.

Momentum-dependent distribution function is given by

$$\langle n_{\mathbf{k}} \rangle = \frac{1}{2} \sum_{\sigma} \langle c_{\mathbf{k}\sigma}^{\dagger} c_{\mathbf{k}\sigma} \rangle. \quad (\text{A1})$$

Pomeranchuk order parameters, $\xi_{d_{x^2-y^2}}$ and $\xi_{d_{xy}}$, which quantify the amount of symmetry breaking [36], are given on the triangular lattice as [35]

$$\xi_{d_{x^2-y^2}} = \sum_{\mathbf{k}} d_{x^2-y^2}(\mathbf{k}) n_{\mathbf{k}}, \quad (\text{A2})$$

$$\xi_{d_{xy}} = \sum_{\mathbf{k}} d_{xy}(\mathbf{k}) n_{\mathbf{k}}, \quad (\text{A3})$$

where $\sum_{\mathbf{k}} = 1$. The form factors, $d_{x^2-y^2} = \cos(k_x) - \cos(\sqrt{3}k_y/2) \cos(k_x/2)$ and $d_{xy} = \sqrt{3} \sin(\sqrt{3}k_y/2) \sin(k_x/2)$, describe the component-resolved distortion of d -wave instabilities for the Fermi surface distortion in the point group C_6 . When the C_6 symmetry is preserved, both $\xi_{d_{x^2-y^2}}$ and $\xi_{d_{xy}}$ are equal to zero.

Static spin and charge susceptibilities. The static spin susceptibility reads

$$\chi_s(\mathbf{k}) = 2 \int_0^{\beta} d\tau \langle S_{\mathbf{k}}^z(\tau) S_{-\mathbf{k}}^z(0) \rangle, \quad (\text{A4})$$

where τ denotes imaginary time and β is the inverse temperature, while the static charge susceptibility is given by

$$\chi_c(\mathbf{k}) = \int_0^{\beta} d\tau \langle n_{\mathbf{k}}(\tau) n_{-\mathbf{k}}(0) \rangle. \quad (\text{A5})$$

The local spin susceptibility is then given by

$$\chi_s^{\text{loc}} = \sum_{\mathbf{k}} \chi_s(\mathbf{k}), \quad (\text{A6})$$

while the DMFT impurity spin susceptibility is calculated as

$$\chi_s^{\text{imp}} = \frac{\chi_0(0)}{1 - U\chi_0(0)}, \quad (\text{A7})$$

where the polarization function is $\chi_0(0) = -\sum_{\omega_n} G^{\text{imp}}(i\omega_n)G^{\text{imp}}(-i\omega_n)$, with G^{imp} being the DMFT impurity Green's function and $\sum_{\omega_n} = 1$.

Exponent of the impurity self-energy. To quantify non-Fermi liquid behavior we can fit the imaginary parts of the DMFT self-energies at small Matsubara frequencies (ω_n) to

$$|\text{Im}\Sigma_{\text{DMFT}}(i\omega_n)| \propto \omega_n^\alpha. \quad (\text{A8})$$

For Fermi liquids, $\text{Im}\Sigma(i\omega_n) \propto \omega_n$ with the exponent $\alpha = 1$ on the Matsubara axis (i.e., $\text{Im}\Sigma(\omega) \propto \omega^2$ on the real frequency axis). If $\alpha < 0.5$, the bad metallic behavior is indicated as a signature of non-Fermi liquid.

Superconducting gap functions. For pairing instabilities we solve the linearized Eliashberg equation to find leading eigenvalues λ and superconducting gap functions Δ as

$$\lambda\Delta(k) = -\frac{1}{\beta} \sum_{k'} V_{\text{eff}}(k-k')G(k')G(-k')\Delta(k'), \quad (\text{A9})$$

where $k = (\mathbf{k}, i\omega_n)$ with the fermionic Matsubara frequency ω_n , G denotes the single-particle Green's function, and the effective interaction for the spin-singlet pairing,

$$V_{\text{eff}}(k) = U + \frac{3}{2}U^2\chi_s(k) - \frac{1}{2}U^2\chi_c(k). \quad (\text{A10})$$

In this paper, we focus ourselves on even-frequency gap functions with even parity in the Matsubara frequency, which satisfy $\Delta(\mathbf{k}, i\omega_n) = [\Delta(\mathbf{k}, i\omega_n) + \Delta(\mathbf{k}, -i\omega_n)]/2$. Superconductivity is identified when the largest eigenvalue λ exceeds unity.

Appendix B: Ideal partially flat-band model

In this section, we explore how the way in which the flat portion in the band dispersion is prepared affects the physics. So here we introduce the Hubbard model on a model [which we call the ideal partially flat-band (iPFB)] with a truncated dispersion given as

$$\varepsilon_{\mathbf{k}}^{\text{iPFB}} = -\frac{W}{W_\kappa} \times \begin{cases} \varepsilon_{\mathbf{k},0} & \varepsilon_{\mathbf{k},0} < \kappa, \\ \kappa & \text{otherwise.} \end{cases} \quad (\text{B1})$$

Namely, the dispersion is made perfectly flat for energies below κ for a tight-binding model having a nearest-neighbor t and second-neighbor t' with the dispersion,

$$\begin{aligned} \varepsilon_{\mathbf{k},0} = & -t[2\cos(k_x) + 4\cos(k_x/2)\cos(\sqrt{3}k_y/2)] \\ & -t'[2\cos(\sqrt{3}k_y) + 4\cos(3k_x/2)\cos(\sqrt{3}k_y/2)], \end{aligned} \quad (\text{B2})$$

see Fig. S1(a). Thus the larger the κ , the more extended the flat region. We have here inverted the signs of t and t' to put the van Hove singularity near the band bottom for the triangular lattice (occupied at small band fillings). The band width is that of Eq.(C2) minus κ . Here we take the band width to be $W = 7.533t$.

1. Results for iPFB

Let us present the numerical result for iPFB, here for $U = 4.5t$ and, except in Figs. S4(d), S7(b), S12(a), the inverse temperature is $\beta = 1/(k_B T) = 30/t$. We take t as the unit of energy as in the main text.

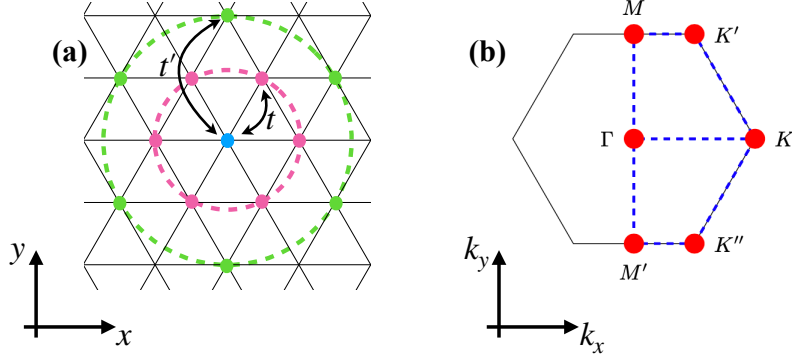


Figure S1. (a) Triangular lattice. Hopping from a lattice point (blue dot) to the nearest neighbors (pink) with an amplitude t , and to the second neighbors (green) with t' . (b) Hexagonal Brillouin zone for the triangular lattice with high symmetry points marked. M and M' are equivalent, in twofold (in the presence of the nematicity) as well as sixfold (in its absence) rotational symmetries. In the presence of sixfold symmetry, K' and K'' are equivalent.

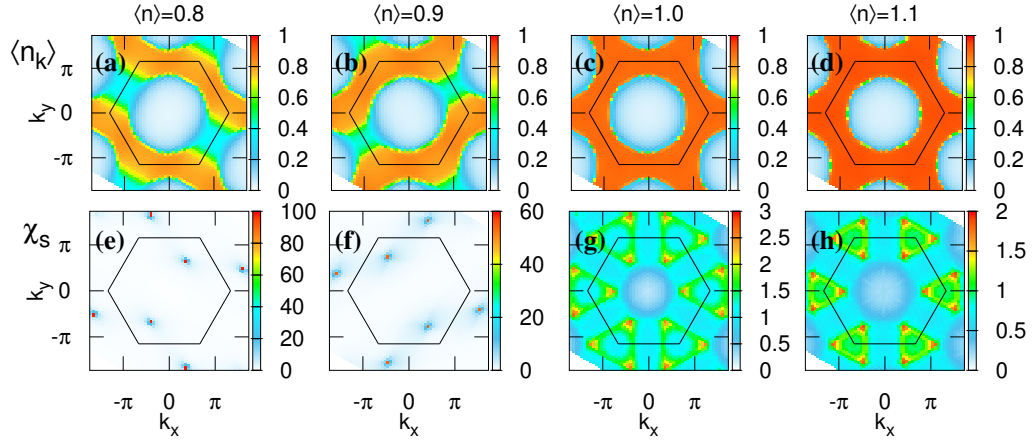


Figure S2. For the iPFB model, here with $\kappa = 1.0$ and $U = 4.5$, momentum distribution functions (top panels) and spin susceptibilities (bottom) are presented in momentum space for band fillings $\langle n \rangle = 0.8$ (a, e, i), 0.9 (b, f, j), 1.0 (c, g, k) and 1.1 (d, h, l). The black hexagon in each panel represents the Brillouin zone. Note different color codes for different band fillings.

a. Nematicity and non-Fermi liquid behavior

In search for footprints of non-Fermi liquid behavior, we start with the absolute value of Green's functions $|G_{\mathbf{k}}|^2$ (top rows) and the momentum-dependent occupation number (middle) in Figs. S2, S3 for the iPFB models with $\kappa = 1.0$ and 1.5 . The iPFB model displays an absence of sharp peaks in $|G_{\mathbf{k}}|^2$ as for $t' = 0$ (not shown), i.e., absence of well-defined Fermi surfaces, which hints that non-Fermi physics governs these systems. A further signature of non-Fermi liquid characters is evident in $\langle n_{\mathbf{k}} \rangle$ in which we observe $\max[\langle n_{\mathbf{k}} \rangle] < 0.95$ for all presented band fillings in the iPFB model.

In the hole-doped regime of the iPFB model with $\kappa = 1.0$, we observe a broken sixfold symmetry, see panels (a,b) and (e,f) in Fig. S2. For $\kappa = 1.5$ in Fig. S3, the reduction from C_6 to C_2 occurs even at half-filling, while the symmetry is resumed for smaller band fillings, namely $\langle n \rangle < 0.8$. These results suggest that the onset of broken C_6 symmetry is shifted to higher band fillings as we increase the size of the flat portion. Thus we can conclude that the spontaneous nematicity occurs both in the PFB and iPFB, even though the detail of band dispersion is significantly different between the two models.

If we look at the normalized double occupancy against band filling in Fig. S4(a) to see how this quantity is correlated with the spontaneous breaking of C_6 . Above a particular filling, the normalized double occupancy in systems with (dashed curves) and without (solid curves) enforced C_6 symmetry are identical. Below this critical band filling, which we call $\langle n_c \rangle$, the Pomeranchuk instability occurs as a first-order phase transition. Figure S4(a) shows that $\langle n_c \rangle$ (marked as vertical lines for the respective values of κ) depends systematically on the size of the flat portion

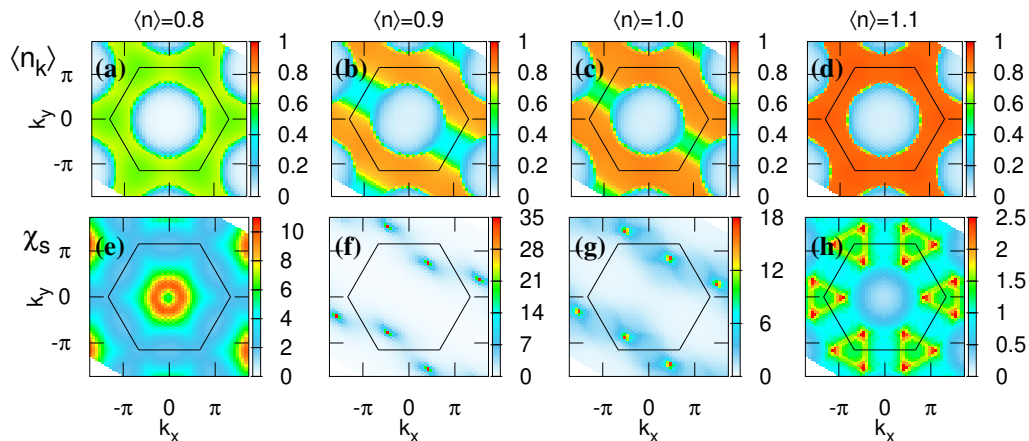


Figure S3. The same as the previous figure, for an increased $\kappa = 1.5$.

as $\langle n_c \rangle = 0.91$ for $\kappa = 0$, $\langle n_c \rangle = 0.97$ for $\kappa = 1.0$, and $\langle n_c \rangle = 1.08$ for $\kappa = 1.5$. For $\kappa = 1.5$, if we further decrease the filling to $\langle n \rangle < 0.8$ the C_6 symmetry is restored as we have already noted in Fig.S3. We refer to $\langle n_{cl} \rangle = 0.81$ as the lower critical filling.

We can also note that we have a Lifshitz transition at the critical band filling $\langle n_c \rangle$, i.e., the closed ridges in $|G_{\mathbf{k}}|^2$ above $\langle n_c \rangle$ are topologically changed to an open structure, c.f. panels(b,c) in Fig. S2 and (c,d) in Fig. S3. The second Lifshitz transition occurs at the lower $\langle n_{cl} \rangle$, below which the open ridges in $|G_{\mathbf{k}}|^2$ resume a closed structure, see Fig. S3(a).

If we actually examine in Fig. S4(b) the Pomeranchuk order parameters (ξ s) against band filling for κ increased from 0 to 1.5 at $\beta = 30$. For $\kappa = 0$, $\xi_{d_{xy}}$ (light green squares) and $\xi_{d_{x^2-y^2}}$ (dark green circles) experience a first-order phase transition at a $\langle n_c \rangle$. Below this critical filling, both orders grow, with $\xi_{d_{xy}}$ larger of the two. For $\kappa = 1.0$, we observe a sharp rise in $\xi_{d_{x^2-y^2}}$ at a shifted $\langle n_c \rangle$ accompanied by a sharp rise in $\xi_{d_{xy}}$ at $\langle n_{c2} \rangle = 0.964$ (vertical dotted orange line). When κ is increased to 1.5, the critical band filling $\langle n_c \rangle$ for $\xi_{d_{x^2-y^2}}$ further increases, while $\xi_{d_{xy}}$ has a jump at $\langle n_{c2} \rangle = 1.027$ (vertical dotted sky-blue line) accompanied by a drop in $\xi_{d_{x^2-y^2}}$. For $\langle n \rangle < \langle n_{c2} \rangle$, the dominant Pomeranchuk instability has d_{xy} character. This continues until the lower critical filling $\langle n_{cl} \rangle = 0.81$ below which the iPFB system retrieves the C_6 symmetry and all instabilities are gone.

We now look at their temperature dependence of ξ s at respective $\langle n_c \rangle$ in Fig. S4(d). For $\kappa = 0$, the rapid growth of both $\xi_{d_{x^2-y^2}}$ and $\xi_{d_{xy}}$ simultaneously occur around $T \approx 0.05$. It is evident that these nematic orders at $\langle n_c \rangle$ survive at higher temperatures with $\xi_{d_{xy}}$ remaining dominant. For $\kappa = 1.0$, we see a first-order phase transition in $\xi_{d_{x^2-y^2}}$ at $T \approx 0.038$ followed by a sharp increase in $\xi_{d_{xy}}$ at $T \approx 0.055$. At $T = 0.066$, the two Pomeranchuk instabilities become comparable. For $\kappa = 1.5$, we witness a first-order phase transition for $\xi_{d_{x^2-y^2}}$ at $T \approx 0.038$, dark blue line in Fig. S4(d). This order parameter remains the only instability at higher temperatures as at $\langle n_c \rangle$, with $\xi_{d_{xy}}$ almost vanishing as the temperature is increased.

We turn to the spin susceptibility in Figs. S2, S3(bottom rows) for $\kappa = 1.0$ and 1.5, respectively. In the electron-doped regime where the Pomeranchuk distortion is absent, the spin susceptibility exhibits spikes corresponding to antiferromagnetic spin structure at $\mathbf{k} = (\sqrt{3}\pi/2, 0)$ with its equivalent sixfold k-points. Below $\langle n_c \rangle$, the spin susceptibility exhibits two streaks, reflecting the C_2 symmetry. These are centered around $\mathbf{k} = (\sqrt{3}\pi/3, 2\pi/3)$, and its twofold equivalent places. At $\langle n \rangle = 0.9$ for $\kappa = 1.0$, the streaks in the spin susceptibility are rotated by $\pi/6$ and located at $\mathbf{k} = (-\sqrt{3}\pi/3, 2\pi/3)$, and its twofold equivalent places. For $\kappa = 1.5$, we can confirm that the sixfold symmetry is resumed in the spin susceptibility as well below $\langle n \rangle = \langle n_{cl} \rangle$. In agreement with the conclusion of the main text, we can thus infer that the nematicity is triggered by spin fluctuations.

We can further look at the impurity and local spin susceptibilities in Fig. S5(a,b), respectively. Right at $\langle n \rangle = \langle n_c \rangle$, the χ_s^{imp} and χ_s^{loc} in systems without the enforced C_6 symmetry exhibit drastic deviations from the C_6 -imposed results. At $\langle n_{c2} \rangle$ with $\kappa = 1.0$ and 1.5 where the dominant instability changes from $\xi_{d_{x^2-y^2}}$ to $\xi_{d_{xy}}$, the impurity and local spin susceptibilities exhibit small kinks.

In addition, at fillings below $\langle n_c \rangle$ (solid vertical lines in Fig. S5), the difference between χ_s^{loc} in the presence (dashed lines) and absence (solid) of C_6 becomes more pronounced as the flat-band region is widened. This is as expected, since the many-body effects, reflected in $\chi_s(\mathbf{k})$, are stronger in partially flat band systems. This property has also been noticed for partially flat-band systems studied with the determinant Monte-Carlo [8] and FLEX+DMFT [9]

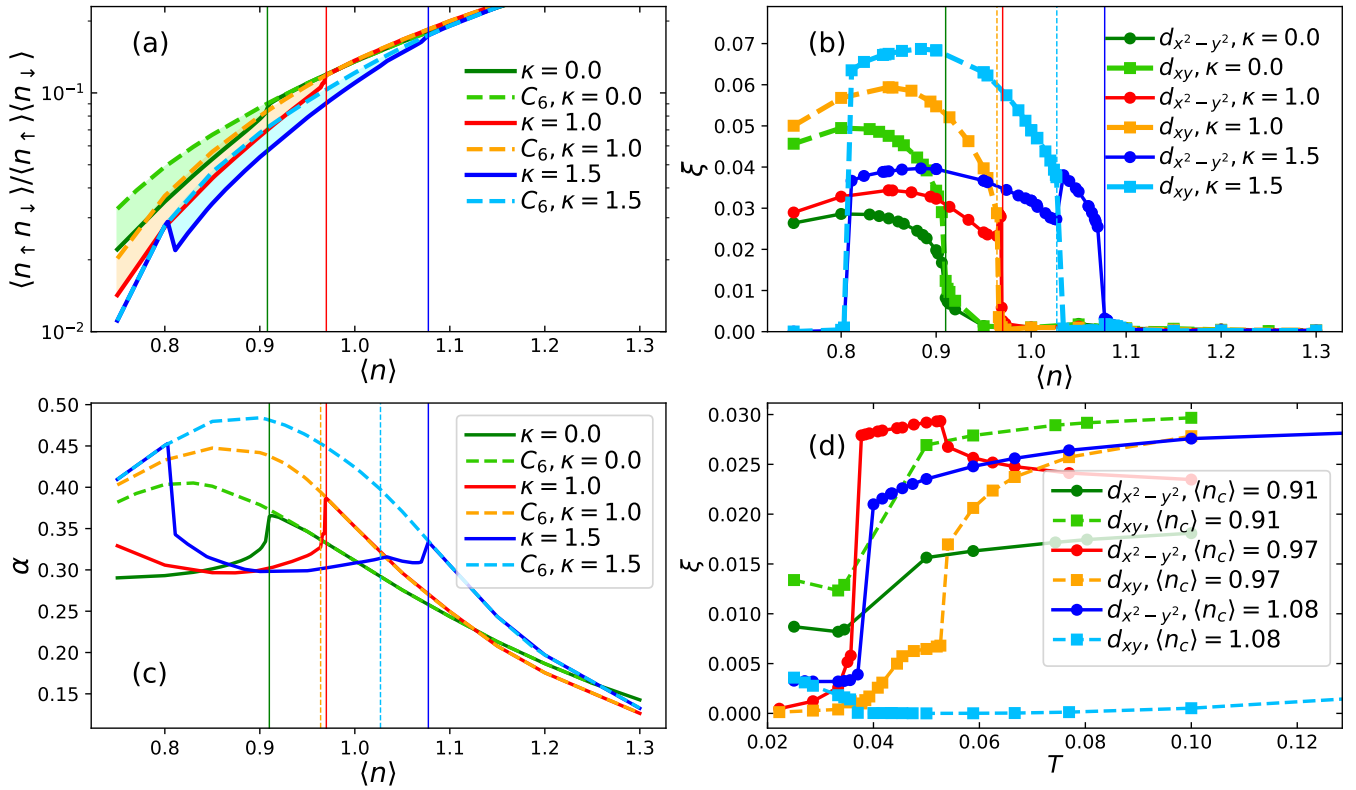


Figure S4. For iPFB (a) normalized double occupancy against the band filling for various values of κ with (dashed curves) and without (solid curves) enforced C_6 symmetry. Shaded areas mark the deviation between the two cases. (b) Pomeranchuk order parameters ξ for various values of κ . (c) The exponent α of the impurity self-energy at $\beta = 30$. Dashed curves represent the case of enforced C_6 . We take $\beta = 30$ for these panels. (d) The Pomeranchuk order parameters at respective $\langle n \rangle = \langle n_c \rangle$ against temperature for various values of κ (with the same color code as in (a)). Vertical solid (dashed) lines mark $\langle n_c \rangle$ ($\langle n_{c_2} \rangle$), respectively.

calculations on the square lattice.

To further track the fingerprints of the nematic orders, we present in Fig. S6 the momentum-dependent spectral function, $A(\mathbf{k}, \omega)$, in iPFB with $\kappa = 1.0$ (b) or $\kappa = 1.5$ (c) at $\langle n \rangle = 0.9$. In the presence of the interaction, the flat region at the bottom of the bands seen in $A(\mathbf{k})$ changes little, aside from a downward energy shift, except along the high symmetry lines where C_6 is broken as identified in Figs. S2, S3. More specifically, for $\kappa = 1.0$, the nematicity vector is along $K' \rightarrow K$, which changes to $K \rightarrow K''$ for $\kappa = 1.5$, see labels in Fig. S1(b). For the momenta in these regions, the spectral function splits with a gap $\lesssim U/2$.

To corroborate the non-Fermi liquid character of electrons in our models, we plot the exponent α of the impurity self-energies in systems with (dashed lines) and without (solid) the sixfold symmetry in Fig. S4(c) above. For the whole band-filling region studied, α exhibits values less than 0.5, indicating non-Fermi liquids. In the electron-doped regime for $\langle n \rangle > \langle n_c \rangle$ with unbroken C_6 , α grows as we approach $\langle n_c \rangle$ as the band filling is decreased. Just below $\langle n_c \rangle$, α exhibits a sharp drop, followed by a gradual enhancement accompanying the Pomeranchuk instabilities. Close to $\langle n \rangle = \langle n_{c_2} \rangle$, α in the presence of nematicity (solid lines) undergoes another drastic reduction.

b. Superconductivity

We now turn to superconductivity in the iPFB. We present the largest eigenvalue λ of the Eliashberg equation for the singlet pairing in Fig. S7(a). If we first look at the result when the C_6 symmetry is imposed (dashed lines), λ remains below 0.85, i.e., no superconducting instabilities. Similar to our finding in the main text for the PFB model, we can characterize the double-dome structure in λ as a signature of a change in the number of nodal lines from 2 in the right dome to ≥ 4 for the left dome. The band filling at which these two domes are connected is indicated by arrows with the same color as the corresponding dashed lines in Fig. S7(a). When the nematicity is allowed,

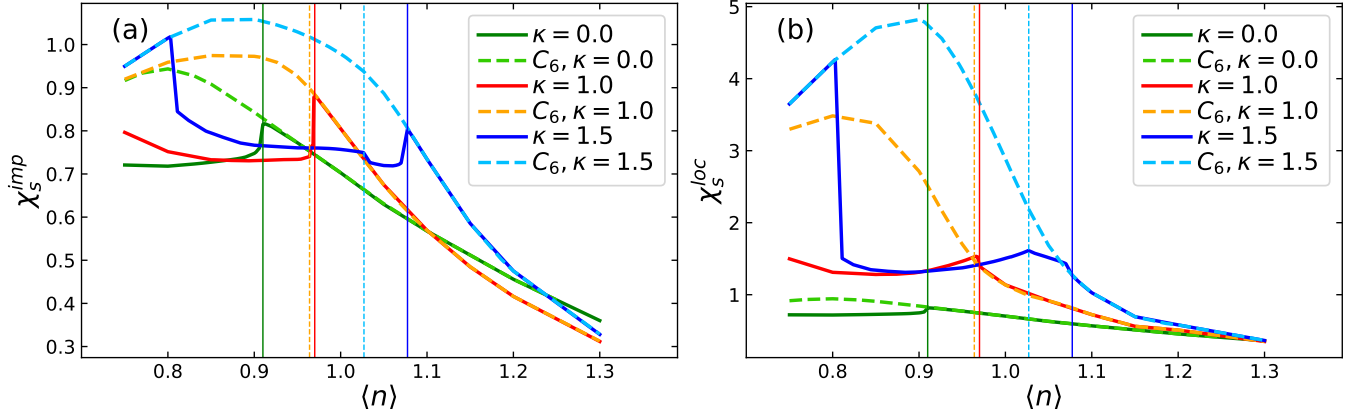


Figure S5. Impurity spin susceptibility (a) and local spin susceptibility (b) for the regular band model with $\kappa = 0$ (green lines), and for the iPFB models with $\kappa = 1.0$ (red lines) or 1.5 (blue lines). Dashed lines represent the results with the imposed sixfold symmetry. Vertical solid (dashed) lines mark $\langle n_c \rangle$ ($\langle n_{c2} \rangle$).

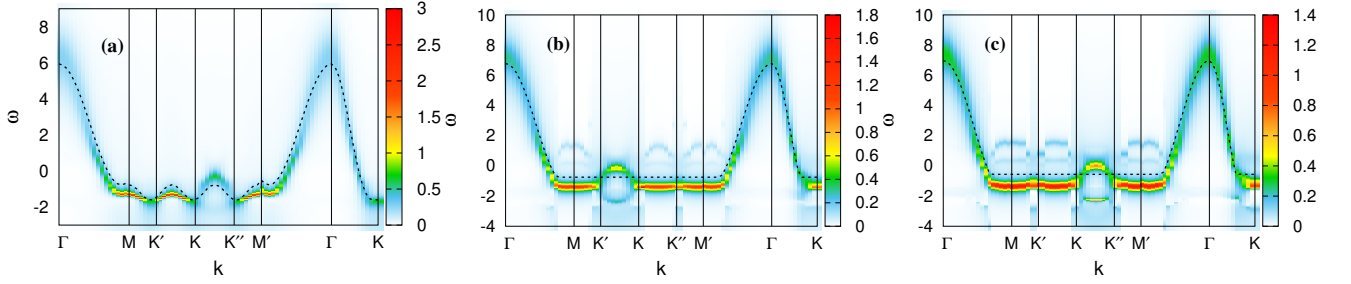


Figure S6. Momentum-dependent spectral function along high-symmetry momenta for $\kappa = 1.0$ (b) or 1.5 (c) at $\langle n \rangle = 0.9$. Dashed black line in each panel represents the noninteracting band structure shifted by the chemical potential $\mu = -0.73$ (b), or -0.91 (c).

in a sharp contrast, λ becomes significantly higher, and specifically rapidly exceeds unity just below the respective $\langle n_c \rangle$. After this peak, λ decreases as the filling is decreased, until a second rise occurs at $\langle n \rangle = \langle n_{c2} \rangle$, followed by a second decrease. Corresponding superconducting transition temperatures is displayed in Fig. S7(b). The double-dome structure is inherited in T_c , which endorses the interplay between various symmetries of Pomeranchuk distortions and the superconducting instabilities.

To identify the pairing symmetry, we present the singlet gap functions in momentum and real spaces for the regular band in Fig. S8, for iPFB model with $\kappa = 1.0$ in Fig. S9, and for $\kappa = 1.5$ in Fig. S10. Above $\langle n_c \rangle$, the gap functions have $d_{x^2-y^2}$ symmetry [see panels (d) in these figures], where the pairing in real-space extends to one lattice spacing [panels (h)]. As in Fig. 4 in the main text for PFB, the gap function changes from the $d_{x^2-y^2}$ -wave to a $\gamma s_{x^2+y^2} - d_{x^2-y^2} - d_{xy}$ -wave for $\langle n_{c1} \rangle < \langle n \rangle < \langle n_c \rangle$ when Pomeranchuk distortions emerge, see panels (a,b) in Fig. S8 for the regular band, panel (a) in Fig. S9 and panels (a,b) in Fig. S10 for iPFB. The value of γ increases from zero to almost 0.3 when the filling is reduced from $\langle n_c \rangle$ up to $\langle n_{c2} \rangle$. γ acquires values larger than 0.3 below $\langle n_{c2} \rangle$. In iPFB with $\kappa = 1.0$ at $\langle n \rangle = 0.9$ the superconducting gap function exhibits a $\pi/6$ rotated $s_{x^2+y^2} - d_{x^2-y^2} - d_{xy}$ -wave pairing, i.e., $s_{x^2+y^2} - d_{x^2-y^2} + d_{xy}$ -wave pairing, which reflects the momentum-dependency of its spin-susceptibility. Below $\langle n_{c1} \rangle$, the pair becomes spatially extended (panel (e) in Fig. S10), which accompanies the appearance of multiple nodal lines in the k-space (panel (a)). While this is expected for the systems with partially flat bands [9] because of a bunch of pair-scattering channels around the flat regions, suppression of these types of pairings in the presence of Pomeranchuk instabilities is interesting. This can be understood by recalling that a nematicity, which brings about some superstructures, degrades the flatness of the noninteracting band dispersion. Concomitantly, the spin susceptibility acquires spikes structures.

Aside from the discussed singlet superconductivity, we have also examined the triplet gap functions and associated λ . Our results show that the λ never exceeds 0.4 in the region studied. This is why we have not presented these data in the present work.

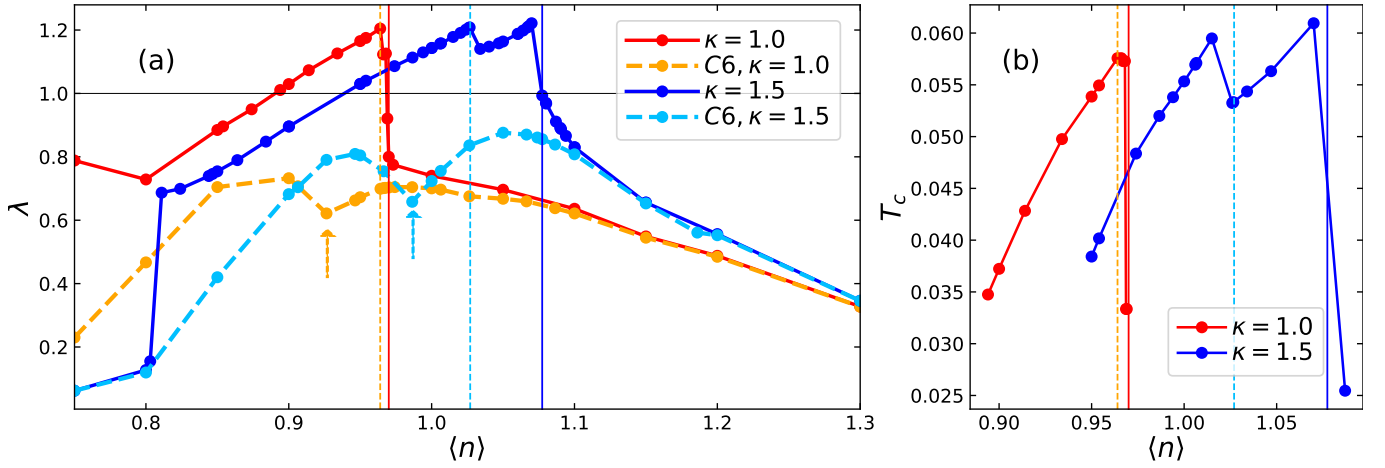


Figure S7. For the iPFB with $\kappa = 1.0$ (red lines) or $\kappa = 1.5$ (dark blue) the linearized Eliashberg eigenvalue λ (a) and superconducting transition temperature T_c (b) are plotted. In (a) dashed lines show λ when the sixfold symmetry is imposed, the black horizontal line marks $\lambda = 1$, and arrows point to respective dips when the C_6 constraint is enforced. Vertical solid lines indicate respective $\langle n_c \rangle$, while dotted vertical lines mark respective $\langle n \rangle = \langle n_{c_2} \rangle$.

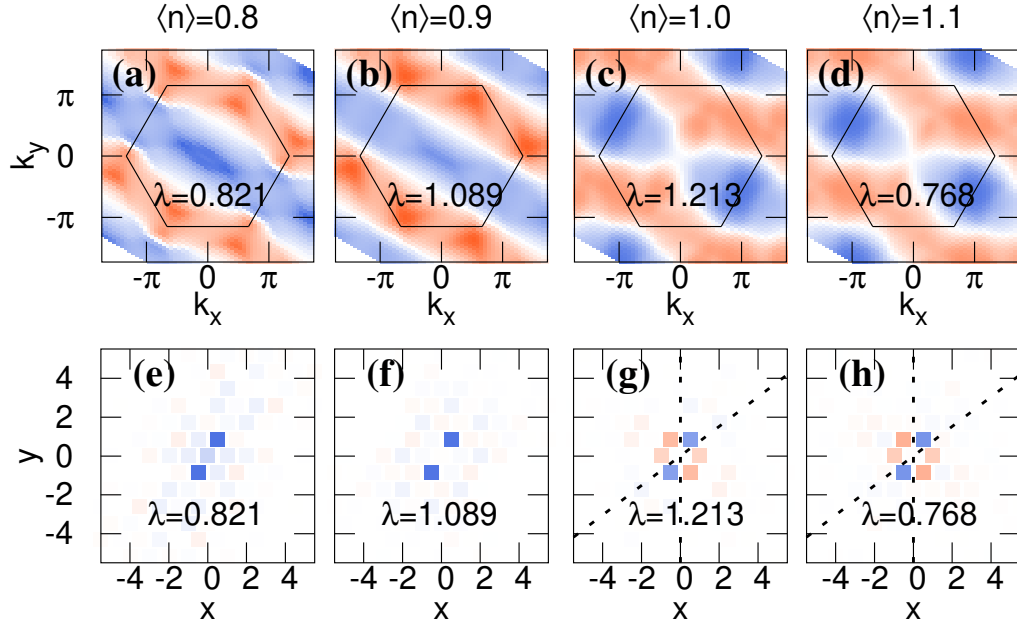


Figure S8. Singlet gap functions in momentum-space (top row) and in real-space (bottom) for the regular band with $t' = 0$ and $\kappa = 0$. Black hexagons in top panels indicate the Brillouin zone. Dashed lines in panels (g,h) represent nodes.

Appendix C: Density of states for triangular lattices

To demonstrate presence of van-Hove singularities in our triangular lattices, we present in Fig. S11 the noninteracting density of states (DOS) for the regular band with $t' = 0$ (solid green line in panel (a)), PFB with $t' = 0.15$ (dashed blue line in panel (a)), and iPFB with $\kappa = 1.0$ (solid green line in panel (b)), or $\kappa = 1.5$ (dashed blue line in panel (a)). The DOS for the system with a partially flat portion, the blue line in panel (a) and lines in panel (b), exhibit a singular value as small energies. A large DOS is also observed at $\omega \approx -1.68$, slightly above the bottom of the band, for the regular band system. Note that while the bandwidths of these four systems are identical, the bottom of their band structure is not located at the same energy.

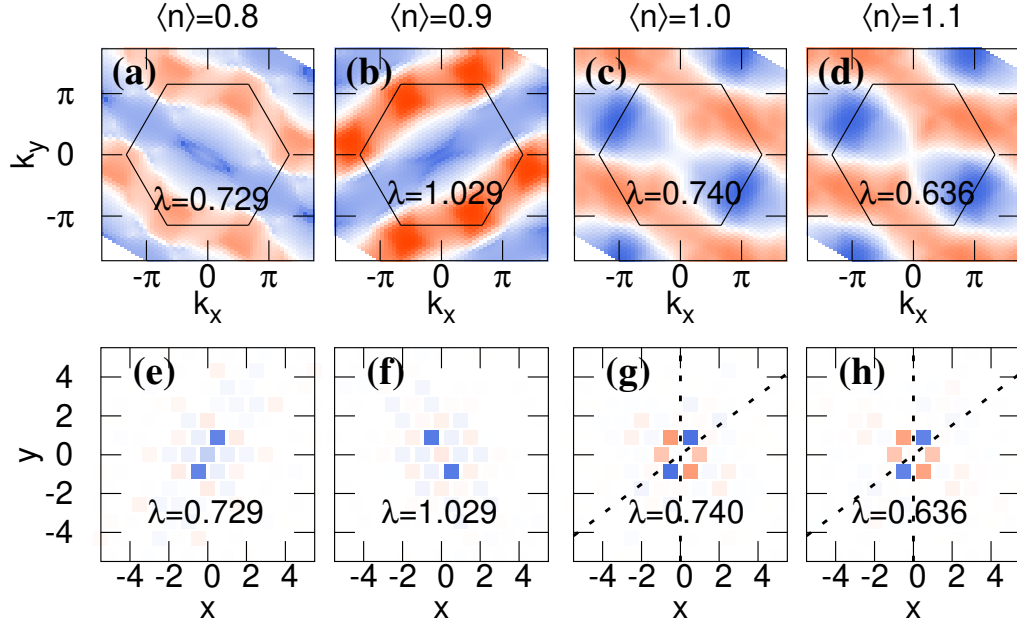


Figure S9. Singlet gap functions in momentum-space (top row) and in real-space (bottom) for iPFB with $\kappa = 1.0$. Black hexagons in top panels indicate the Brillouin zone. Dashed lines in panels (g,h) represent nodes.

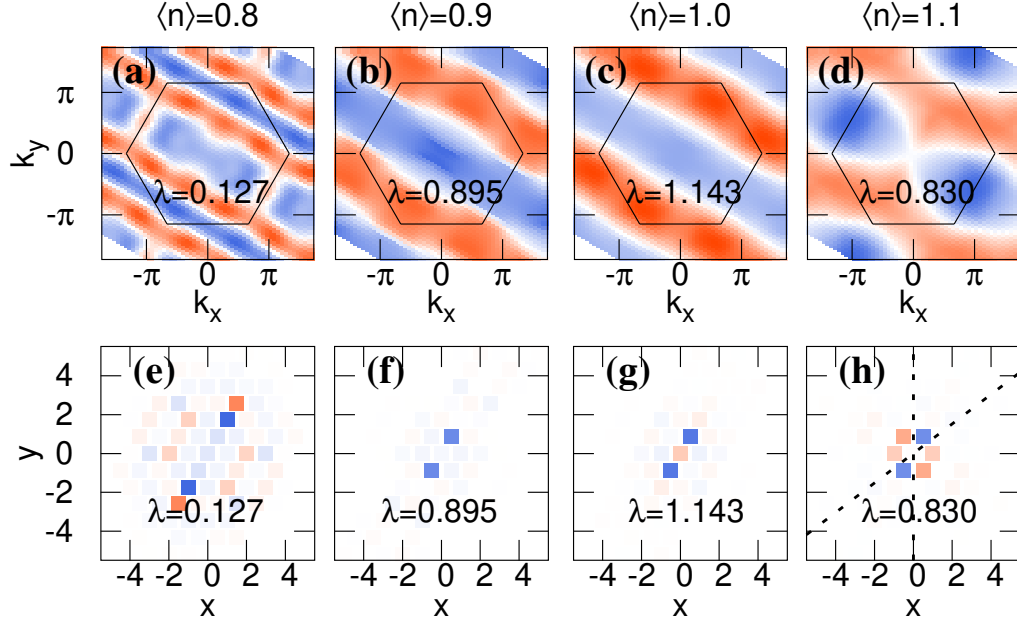


Figure S10. The same as above figure for an increased $\kappa = 1.5$.

Appendix D: Further details on the PFB model

1. Pomeranchuk order parameters at $\langle n_c \rangle$

To further explore the temperature-dependence of the Pomeranchuk instabilities, we plot $\xi_{d_{x^2-y^2}}$ and $\xi_{d_{xy}}$ at $\langle n_c \rangle$ against temperature in Fig. S12(a). While for $T < 0.0425$ both of the nematic orders are negligible, $\xi_{d_{x^2-y^2}}$ undergoes a first-order transition at $T = 0.0425$, which indicates the broken C_6 symmetry at higher temperatures.

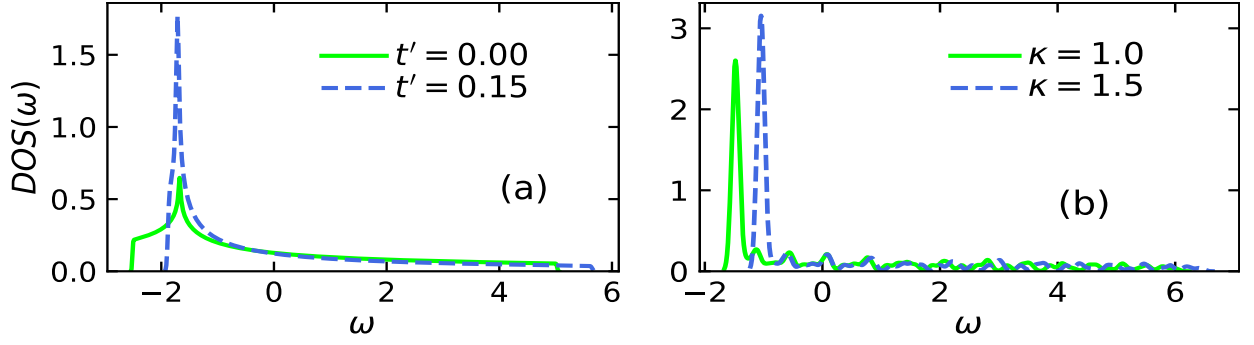


Figure S11. Noninteracting density of states in the regular band model with $t' = 0$ [solid green line in panel (a)], the PFB model with $t' = 0.15$ [dashed blue line in (a)], the iPFB model with $\kappa = 1.0$ [solid green line in (b)], or with $\kappa = 1.5$ [dashed blue line in (b)]. Note different ranges in the plot between (a) and (b).

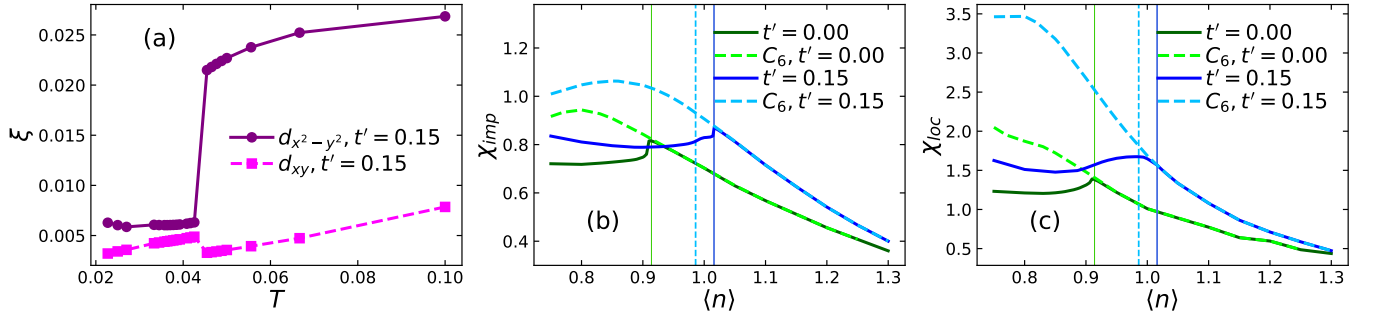


Figure S12. (a) For the PFB model Pomeranchuk order parameters, $\xi_{d_{x^2-y^2}}$ (solid purple line) and $\xi_{d_{xy}}$ (pink), at a band filling $\langle n_c \rangle = 1.02$. Impurity (b) and local (c) spin susceptibilities against band filling are also plotted. All panels are for $U = 4.5$ and $\beta = 30$. Vertical solid lines in panels (b,c) indicate $\langle n_c \rangle$, while vertical dotted pale-blue lines $\langle n \rangle = \langle n_{c_2} \rangle$ (see text).

2. Impurity spin-susceptibility

Impurity spin-susceptibility for PFB model with $t' = 0.15$ in Fig. S12(b) shows that the increasing spin fluctuations for $\langle n \rangle > \langle n_c \rangle$ sharply drops when sixfold rotational symmetry is broken for $\langle n \rangle < \langle n_c \rangle$. Local spin-susceptibility in Fig. S12(c), on the other hand, displays a maximum at $\langle n \rangle = \langle n_{c_2} \rangle$ in PFB. We can note that we hardly detect any features at $\langle n_{c_2} \rangle$ in the impurity spin-susceptibility which might be related to a crossover from $\xi_{d_{x^2-y^2}}$ to $\xi_{d_{xy}}$, see Fig. S12(a). When the structure of ξ undergoes an abrupt change from $\xi_{d_{x^2-y^2}}$ to $\xi_{d_{xy}}$, due to the first-order transition in $\xi_{d_{xy}}$, the impurity spin-susceptibility exhibits a kink at $\langle n_{c_2} \rangle$, see e.g. Fig. S4(b) and related discussion in Sec. B.

Appendix E: Dependency of the critical band filling on the Hubbard interaction

To explore the relation between $\langle n_c \rangle$ and the Hubbard interaction, we present normalized double occupancies and Pomeranchuk order parameters for three different U values in Fig. S13. The sixfold symmetry of the triangular lattice remains unbroken for the PFB systems with $t' = 0.15$ and $U = 2.5$ as can be seen both from the renormalized double occupancy, green lines in panel (a), and also from zero Pomeranchuk instabilities, green lines in panel (b). The C_6 symmetry is broken at larger Hubbard interactions, namely $U = \{3.5, 4.5\}$, as shown by red and blue lines in Fig. S13, respectively. The critical band filling $\langle n_c \rangle$ for the PFB systems with $U = 3.5$ is 0.9 (red vertical lines).

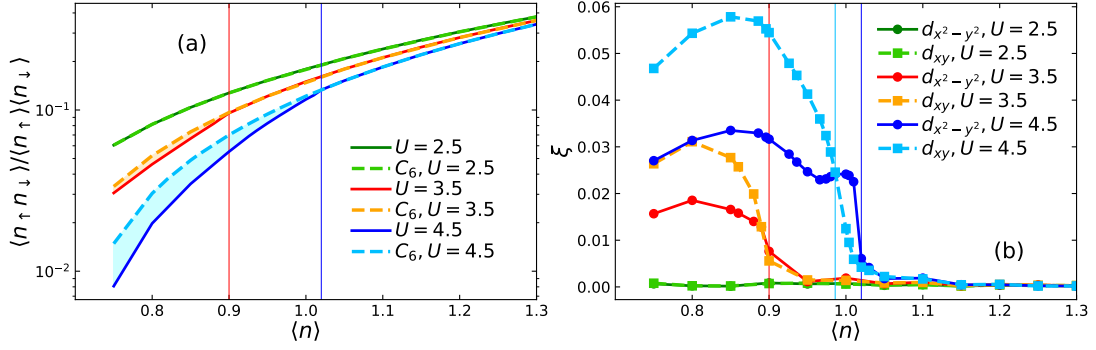


Figure S13. Normalized double occupancy (a) and Pomeranchuk order parameter (b) for the PFB systems with $t' = 0.15$, $U = 2.5$ (green lines), 3.5 (red lines), and 4.5 (blue lines) and at $\beta = 30$. Dashed lines in panel (a) describe normalized double occupancies for systems with the imposed sixfold symmetry. $\xi_{d_{x^2-y^2}}$ and $\xi_{d_{xy}}$ are presented with solid and dashed lines in panel (b), respectively. Vertical lines indicate $\langle n_c \rangle$.

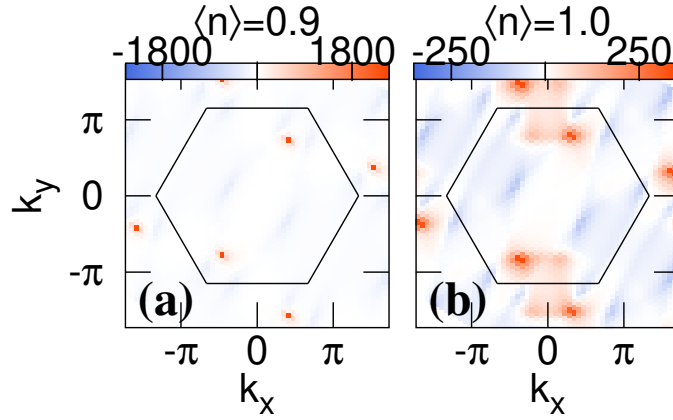


Figure S14. Difference, $\Delta V_{\text{eff}} = V_{\text{eff}} - V_{\text{eff}}^{C_6}$, in the effective pairing interaction between the absence and presence of the C_6 symmetry for the PFB system with $t' = 0.15$ for $U = 4.5$ and $\beta = 30$ for $\langle n \rangle = 0.9$ (a) and 1.0 (b). Black hexagons represent the Brillouin zone. Note that the scale of the color bar differs by orders of magnitude between the panels.

1. Superconductivity

Fig. S14 presents $\Delta V_{\text{eff}} = V_{\text{eff}} - V_{\text{eff}}^{C_6}$, where $V_{\text{eff}}^{C_6}$ is the effective interaction with the imposed C_6 constraint. We can see that ΔV_{eff} displays not only the broken C_6 symmetry but also amplitudes significantly intensified than in the C_6 case. See also the discussion on ΔV_{eff} in the main text.

Gap functions in the real-space with singlet, even-frequency pairing for the PFB model with $t' = 0.15$ is plotted in Fig. S15. In the main text, we presented the $\gamma s - d_{xy}$ -wave symmetry of the gap function below $\langle n_c \rangle$ in the momentum space; see Fig. 4(b-d). Evidently, the electron pairing is short-range in this filling region. This observation is in contrast with the formation of extended Cooper pairs in systems where the C_6 constraint is imposed.

Appendix F: Possible singlet pairing symmetries on the triangular lattice

In this section, we present various symmetries in the gap functions that can be realized on the triangular lattice. In the presence of C_6 symmetry and for the pairs not extending beyond nearest neighbors in real space, the spin-singlet gap functions are either $s_{x^2+y^2}$ -wave or d -wave, with respective forms in k-space,

$$\Delta_{s_{x^2+y^2}}(\mathbf{k}) = \cos(k_x) + 2 \cos(\sqrt{3}k_y/2) \cos(k_x/2), \quad (\text{F1})$$

$$\Delta_{d_{x^2-y^2}}(\mathbf{k}) = \cos(k_x) - \cos(\sqrt{3}k_y/2) \cos(k_x/2), \quad (\text{F2})$$

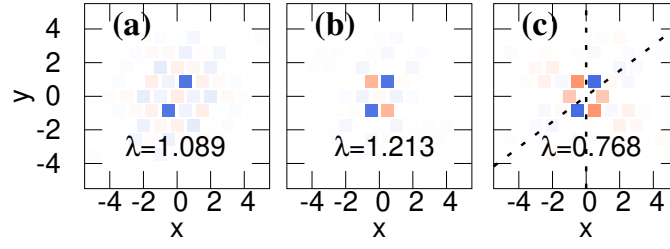


Figure S15. Gap functions in real space with singlet pairing for the PFB system with $t' = 0.15$ for $U = 4.5$ and $\beta = 30$ for $\langle n \rangle = 0.9$ (a), 1.0(b) and 1.1(c). Dashed lines in panel (c) represent nodes. Color code for the gap function is bluish (reddish) for negative (positive) values, for which we have omitted the color bars since the linearized Eliashberg equation does not indicate magnitudes of Δ . This figure is to be compared with Fig. 4(b-d) in the momentum space in the main text.

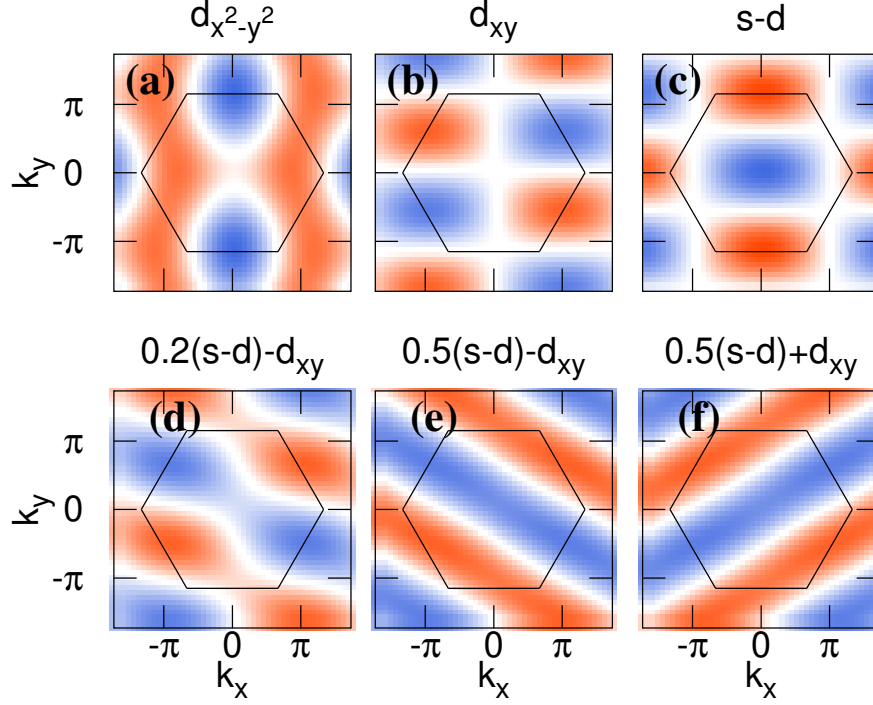


Figure S16. Gap functions $d_{x^2-y^2}$ (a), d_{xy} (b), $s_{x^2+y^2} - d_{x^2-y^2}$ (c), $0.2(s_{x^2+y^2} - d_{x^2-y^2}) - d_{xy}$ (d), $0.5(s_{x^2+y^2} - d_{x^2-y^2}) - d_{xy}$ (e) and $0.5(s_{x^2+y^2} - d_{x^2-y^2}) + d_{xy}$ (f) are plotted in momentum-space, with positive (negative) values represented by blue (red). $s - d$ in panels (c-f) is the shorthand for $s_{x^2+y^2} - d_{x^2-y^2}$.

$$\Delta_{d_{xy}}(\mathbf{k}) = \sqrt{3} \sin(\sqrt{3}k_y/2) \sin(k_x/2). \quad (\text{F3})$$

In the presence of C_6 symmetry, the above two d -waves, depicted in Fig. S16(a-b), are associated with two degenerate irreducible representations in the C_6 point group, so that the topological superconductivity with gap function $\Delta_{d_{x^2-y^2}}(\mathbf{k}) + i\Delta_{d_{xy}}$ is also possible. When C_6 symmetry is reduced down to C_2 , on the other hand, $\Delta_{s_{x^2+y^2}}$ and $\Delta_{d_{x^2-y^2}}$ are no longer irreducible representations, and instead their linear combination $s_{x^2+y^2} - d_{x^2-y^2}$, Δ_{s-d} , with a form factor,

$$\Delta_{s-d}(\mathbf{k}) = 3 \cos(\sqrt{3}k_y/2) \cos(k_x/2), \quad (\text{F4})$$

finds room to emerge, see Fig. S16(c). In the C_2 point group, $s_{x^2+y^2} - d_{x^2-y^2}$ reads s_{y2} , and in this point group s_{y2} and d_{xy} are not degenerate, so that this group does not permit topological superconductivity. Still, linear combinations of $\Delta_{d_{xy}}$ and Δ_{s-d} may be realized, as we have indeed shown in Figs. 4(bottom rows), S8, S9, S10. Fig. S16(d-f) shows $\alpha(s_{x^2+y^2} - d_{x^2-y^2}) + \beta d_{xy}$ with $(\alpha, \beta) = (0.2, -1)$ in (d), $(0.5, -1)$ in (e) and $(0.5, +1)$ in (f). Panel (d) in Fig. S16 exhibits a momentum-dependence similar to Fig. 4(c) on the PFB model at half filling. So this is why we can say the pairing in the PFB model is $s_{x^2+y^2} - d_{x^2-y^2} - d_{xy}$. The structure exemplified by panel (e) is evident in most gap

functions below $\langle n_{c_2} \rangle$ in the regular band, PFB and iPFB models. The gap function in panel (f) is also displayed at $\langle n \rangle = 0.9$ in the iPFB model with $\kappa = 1.0$ in Fig. S9(b).

* sharareh.sayyad@neel.cnrs.fr

† vaezi@sharif.edu

‡ a. These two authors contributed equally

- [1] B Keimer, S A Kivelson, M R Norman, S Uchida, and J Zaanen, “From quantum matter to high-temperature superconductivity in copper oxides,” *Nature* **518**, 179–186 (2014).
- [2] Hideo Hosono and Kazuhiko Kuroki, “Iron-based superconductors: Current status of materials and pairing mechanism,” *Physica C: Superconductivity and its Applications* **514**, 399–422 (2015).
- [3] Flavio S. Nogueira and Enrique V. Anda, “Study on a toy model of strongly correlated electrons,” *International Journal of Modern Physics B* **10**, 3705–3715 (1996).
- [4] Hideo Aoki, “Theoretical possibilities for flat-band superconductivity,” *Journal of Superconductivity and Novel Magnetism* **33**, 2341–2346 (2020).
- [5] Vladyslav Kozii, Hiroki Isobe, Jörn W. F. Venderbos, and Liang Fu, “Nematic superconductivity stabilized by density wave fluctuations: Possible application to twisted bilayer graphene,” *Phys. Rev. B* **99**, 144507 (2019).
- [6] Rafael M. Fernandes and Jörn W. F. Venderbos, “Nematicity with a twist: Rotational symmetry breaking in a moiré superlattice,” *Science Advances* **6**, eaba8834 (2020).
- [7] Bin-Bin Chen, Yuan Da Liao, Ziyu Chen, Oskar Vafek, Jian Kang, Wei Li, and Zi Yang Meng, “Realization of topological mott insulator in a twisted bilayer graphene lattice model,” *Nature Communications* **12** (2021), 10.1038/s41467-021-25438-1.
- [8] Edwin W. Huang, Mohammad-Sadegh Vaezi, Zohar Nussinov, and Abolhassan Vaezi, “Enhanced correlations and superconductivity in weakly interacting partially flat-band systems: A determinantal quantum monte carlo study,” *Phys. Rev. B* **99**, 235128 (2019).
- [9] Sharareh Sayyad, Edwin W. Huang, Motoharu Kitatani, Mohammad-Sadegh Vaezi, Zohar Nussinov, Abolhassan Vaezi, and Hideo Aoki, “Pairing and non-fermi liquid behavior in partially flat-band systems: Beyond nesting physics,” *Phys. Rev. B* **101**, 014501 (2020).
- [10] Noah F. Q. Yuan, Hiroki Isobe, and Liang Fu, “Magic of high-order van Hove singularity,” *Nature Communications* **10** (2019), 10.1038/s41467-019-13670-9.
- [11] T. Itou, Akira Oyamada, S. Maegawa, and R. Kato, “Instability of a quantum spin liquid in an organic triangular-lattice antiferromagnet,” *Nat. Phys.* **6** (2010), 10.1038/nphys1715.
- [12] Satoshi Yamashita, Takashi Yamamoto, Yasuhiro Nakazawa, Masafumi Tamura, and Reizo Kato, “Gapless spin liquid of an organic triangular compound evidenced by thermodynamic measurements,” *Nature communications* **2**, 275 (2011).
- [13] M. Norman, “Herbertsmithite and the search for the quantum spin liquid,” *Reviews of Modern Physics* **88** (2016), 10.1103/RevModPhys.88.041002.
- [14] Ruidan Zhong, Shu Guo, Guangyong Xu, Zhijun Xu, and Robert J. Cava, “Strong quantum fluctuations in a quantum spin liquid candidate with a co-based triangular lattice,” *Proceedings of the National Academy of Sciences* **116**, 14505–14510 (2019).
- [15] Christoph J. Halboth and Walter Metzner, “*d*-wave superconductivity and Pomeranchuk instability in the two-dimensional hubbard model,” *Phys. Rev. Lett.* **85**, 5162–5165 (2000).
- [16] Hiroyuki Yamase and Hiroshi Kohno, “Instability toward formation of quasi-one-dimensional fermi surface in two-dimensional t-j model,” *Journal of the Physical Society of Japan* **69**, 2151–2157 (2000), <https://doi.org/10.1143/JPSJ.69.2151>.
- [17] A. Fedorov, A. Yaresko, T. K. Kim, Y. Kushnirenko, E. Haubold, T. Wolf, M. Hoesch, A. Grüneis, B. Büchner, and S. V. Borisenko, “Effect of nematic ordering on electronic structure of FeSe,” *Scientific Reports* **6**, 1–7 (2016).
- [18] Yann Gallais and Indranil Paul, “Charge nematicity and electronic raman scattering in iron-based superconductors,” *Comptes Rendus Physique* **17**, 113–139 (2016).
- [19] Kyungmin Lee, Jumping Shao, Eun-Ah Kim, F. D. M. Haldane, and Edward H. Rezayi, “Pomeranchuk instability of composite fermi liquids,” *Phys. Rev. Lett.* **121**, 147601 (2018).
- [20] Eduardo Fradkin, Steven A. Kivelson, Michael J. Lawler, James P. Eisenstein, and Andrew P. Mackenzie, “Nematic fermi fluids in condensed matter physics,” *Annual Review of Condensed Matter Physics* **1**, 153–178 (2010).
- [21] Jörn W. F. Venderbos and Rafael M. Fernandes, “Correlations and electronic order in a two-orbital honeycomb lattice model for twisted bilayer graphene,” *Phys. Rev. B* **98**, 245103 (2018).
- [22] J. F. Dodaro, S. A. Kivelson, Y. Schattner, X. Q. Sun, and C. Wang, “Phases of a phenomenological model of twisted bilayer graphene,” *Phys. Rev. B* **98**, 075154 (2018).
- [23] Xiao Chen, S. Maiti, R. M. Fernandes, and P. J. Hirschfeld, “Nematicity and superconductivity: Competition versus cooperation,” *Phys. Rev. B* **102**, 184512 (2020).
- [24] Mohammad Edalati, Ka Wai Lo, and Philip W. Phillips, “Pomeranchuk instability in a non-fermi liquid from holography,” *Phys. Rev. D* **86**, 086003 (2012).
- [25] Paul Malinowski, Qianni Jiang, Joshua J Sanchez, Joshua Mutch, Zhaoyu Liu, Preston Went, Jian Liu, Philip J Ryan,

- Jong-Woo Kim, and Jiun-Haw Chu, “Suppression of superconductivity by anisotropic strain near a nematic quantum critical point,” *Nature Physics* **16**, 1189–1193 (2020).
- [26] Yuan Cao, Daniel Rodan-Legrain, Jeong Min Park, Noah F. Q. Yuan, Kenji Watanabe, Takashi Taniguchi, Rafael M. Fernandes, Liang Fu, and Pablo Jarillo-Herrero, “Nematicity and competing orders in superconducting magic-angle graphene,” *Science* **372**, 264–271 (2021), <https://www.science.org/doi/pdf/10.1126/science.abc2836>.
- [27] A. E. Bohmer, F. Hardy, F. Eilers, D. Ernst, P. Adelman, P. Schweiss, T. Wolf, and C. Meingast, “Lack of coupling between superconductivity and orthorhombic distortion in stoichiometric single-crystalline fese,” *Phys. Rev. B* **87**, 180505 (2013).
- [28] Hiroki Isobe, Noah F. Q. Yuan, and Liang Fu, “Unconventional superconductivity and density waves in twisted bilayer graphene,” *Phys. Rev. X* **8**, 041041 (2018).
- [29] Rafael M. Fernandes, Peter P. Orth, and Jörg Schmalian, “Intertwined vestigial order in quantum materials: Nematicity and beyond,” *Annual Review of Condensed Matter Physics* **10**, 133–154 (2019).
- [30] Mehdi Biderang, Mohammad-Hossein Zare, and Jesko Sirker, “Proximity-driven ferromagnetism and superconductivity in the triangular rashba-hubbard model,” *Phys. Rev. B* **105**, 064504 (2022).
- [31] Motoharu Kitatani, Naoto Tsuji, and Hideo Aoki, “FLEX+DMFT approach to the d -wave superconducting phase diagram of the two-dimensional hubbard model,” *Phys. Rev. B* **92**, 085104 (2015).
- [32] Louis-François Arsenault, Patrick Sémon, and A.-M. S. Tremblay, “Benchmark of a modified iterated perturbation theory approach on the fcc lattice at strong coupling,” *Phys. Rev. B* **86**, 085133 (2012).
- [33] Henrik Kajueter and Gabriel Kotliar, “New iterative perturbation scheme for lattice models with arbitrary filling,” *Phys. Rev. Lett.* **77**, 131–134 (1996).
- [34] A. Vranić, J. Vučićević, J. Kokalj, J. Skolimowski, R. Žitko, J. Mravlje, and D. Tanasković, “Charge transport in the Hubbard model at high temperatures: Triangular versus square lattice,” *Physical Review B* **102**, 1–10 (2020).
- [35] Maximilian L. Kiesel, Christian Platt, and Ronny Thomale, “Unconventional fermi surface instabilities in the Kagome Hubbard model,” *Physical Review Letters* **110** (2013), 10.1103/physrevlett.110.126405.
- [36] Hiroyuki Yamase, Vadim Oganessian, and Walter Metzner, “Mean-field theory for symmetry-breaking Fermi surface deformations on a square lattice,” *Physical Review B* **72**, 1–11 (2005).
- [37] Motoharu Kitatani, *High-Tc Superconductivity studied by diagrammatic extensions of the dynamical mean-field theory*, Ph.D. thesis, University of Tokyo (2017).
- [38] In SM, we show that these spin fluctuations give rise to correlation-driven superstructures in the momentum-dependent spectral functions [48].
- [39] Pierre Massat, Donato Farina, Indranil Paul, Sandra Karlsson, Pierre Strobel, Pierre Toulemonde, Marie Aude Méasson, Maximilien Cazayous, Alain Sacuto, Shigeru Kasahara, Takasada Shibauchi, Yuji Matsuda, and Yann Gallais, “Charge-induced nematicity in FeSe,” *Proceedings of the National Academy of Sciences of the United States of America* **113**, 9177–9181 (2016).
- [40] R. M. Fernandes, A. V. Chubukov, and J. Schmalian, “What drives nematic order in iron-based superconductors?” *Nature Physics* **10**, 97–104 (2014).
- [41] Motoharu Kitatani, Naoto Tsuji, and Hideo Aoki, “Interplay of Pomeranchuk instability and superconductivity in the two-dimensional repulsive hubbard model,” *Phys. Rev. B* **95**, 075109 (2017).
- [42] Philipp Werner, Emanuel Gull, Matthias Troyer, and Andrew J. Millis, “Spin freezing transition and non-fermi-liquid self-energy in a three-orbital model,” *Phys. Rev. Lett.* **101**, 166405 (2008).
- [43] N. S. Vidhyadhiraja, A. Macridin, C. Sen, M. Jarrell, and Michael Ma, “Quantum critical point at finite doping in the 2d hubbard model: A dynamical cluster quantum monte carlo study,” *Phys. Rev. Lett.* **102**, 206407 (2009).
- [44] Hiroshi Ishida and Ansgar Liebsch, “Fermi-liquid, non-fermi-liquid, and mott phases in iron pnictides and cuprates,” *Phys. Rev. B* **81**, 054513 (2010).
- [45] Philipp Werner, Xi Chen, and Emanuel Gull, “Ferromagnetic spin correlations in the two-dimensional hubbard model,” *Phys. Rev. Research* **2**, 023037 (2020).
- [46] We have checked that the values of λ for the spin-triplet even-frequency, singlet and triplet odd-frequency gap functions are much smaller than those for the spin-singlet even-frequency.
- [47] In SM, we present spatially extended pairings, with multi-nodal gap functions for $\langle n \rangle < \langle n \rangle_{\min}$ (marked with a blue arrow in Fig. 3) in PFB with C_6 symmetry [48]. However, such pairings do not form when nematicity is present. As a result, the weight of the real-space gap function in PFB mainly extend to the nearest neighbors.
- [48] The Supplemental Material includes details on ideal partially flat-band systems, further results on PFB model, and details on possible symmetries of singlet gap functions on the triangular lattice.
- [49] Previous studies on the ordinary triangular lattice, with an inverted band structure from the present regular band model, in the strong (electron-electron) coupling regime suggests the chiral $d_{x^2-y^2} + id_{xy}$ superconductivity in an hole-doped regime as the the doublet $[d_{x^2-y^2}, d_{xy}]$ in the point group C_6 is degenerate [?]. This situation still holds for $\langle n \rangle > \langle n_c \rangle$ in our systems, although T_c is much smaller in this region than for $\langle n \rangle < \langle n_c \rangle$.
- [50] Hiroyuki Yamase, “Pomeranchuk instability as order competing with superconductivity,” *Physica C: Superconductivity and its Applications* **470**, S109–S110 (2010).
- [51] Johan Schött, Inka L. M. Locht, Elin Lundin, Oscar Grånäs, Olle Eriksson, and Igor Di Marco, “Analytic continuation by averaging padé approximants,” *Phys. Rev. B* **93**, 075104 (2016).